1   Revision 1

2 Electronic transitions of iron in almandine-
3 composition glass to 91 GPa

4   Susannah M. Dorfman[1], Sian E. Dutton[2], Vasily Potapkin[3], Aleksandr I. Chumakov[4], Jean-Pascal
5   Rueff[5,6], Paul Chow[7], Yuming Xiao[7], Robert J. Cava[8], Thomas S. Duffy[9], Catherine A.
6   McCammon[3], and Philippe Gillet[10]
7
8   1: Department of Geological Sciences, Michigan State University, East Lansing, MI 48824.
9   2: Department of Physics, University of Cambridge, Cambridge CB3 0HE, UK.
10   3: Bayerisches Geoinstitut, University of Bayreuth, 95440 Bayreuth, Germany.
11   4: European Synchrotron Radiation Facility, BP 220, F-38043 Grenoble, France.
12   5: Synchrotron SOLEIL, L'Orme des Merisiers, BP 48 Saint-Aubin, F-91192 Gif-sur-Yvette,
13   France.
14   6: Sorbonne Universités, UPMC Université Paris 06, Laboratoire de Chimie Physique-Matière et
15   Rayonnement, F-75005, Paris, France.
16   7: HPCAT, Geophysical Laboratory, Carnegie Institution of Washington, Argonne, Illinois
17   60439, USA.
18   8: Department of Chemistry, Princeton University, Princeton, NJ 08544, USA.
19   9: Department of Geosciences, Princeton University, Princeton, NJ 08544, USA.
20   10: Earth and Planetary Science Laboratory, Ecole polytechnique fédérale de Lausanne, Station
21   3, CH-1015 Lausanne, Switzerland.

22 Abstract

23   Valence and spin states of Fe were investigated in a glass of almandine ($Fe_3Al_2Si_3O_{12}$)

24   composition to 91 GPa by X-ray emission spectroscopy and energy- and time-domain

25   synchrotron Mössbauer spectroscopy in the diamond anvil cell. Changes in optical properties,

26   total spin moment and Mössbauer parameters all occur predominantly between 1 bar and ~30

27   GPa. Over this pressure range, the glass changes from translucent brown to opaque and black.

28   The total spin moment of the glass derived from X-ray emission spectroscopy decreases by

29   ~20%. The complementary Mössbauer spectroscopy approaches reveal consistent changes in

30   sites corresponding to 80-90% Fe^{2+} and 10-20% Fe^{3+}. The high-spin Fe^{2+} doublet exhibits a

1

31 continuous decrease in isomer shift and increase in line width and asymmetry. A high-spin Fe^{3+}

32 doublet with quadrupole splitting of ~1.2 mm/s is replaced by a doublet with quadrupole splitting

33 of ~1.9 mm/s, a value higher than all previous measurements of high-spin Fe^{3+} and consistent

34 with low-spin Fe^{3+}. These observations suggest that Fe^{3+} in the glass undergoes a continual

35 transition from a high-spin to a low-spin state between 1 bar and ~30 GPa. Almandine glass is

36 not expected to undergo any abrupt transitions in electronic state at deep mantle pressures.

37 Keywords: silicate glass; spin transitions; Mössbauer spectroscopy; nuclear forward

38 scattering; X-ray emission spectroscopy

1. Introduction

40 The high-pressure behavior of Fe-rich silicate liquids is key to the differentiation of the

41 mantle from a primordial magma ocean (Labrosse et al. 2007; Stixrude et al. 2009; Lee et al.

42 2010) and to understanding possible dense melt-rich regions near the core-mantle boundary

43 (Williams and Garnero 1996). The dynamics of melt in the deep mantle is largely controlled by

44 the behavior of Fe, Earth's densest major elemental component. A density crossover in the deep

45 mantle, with negatively-buoyant Fe-rich silicate melt relative to solid mantle silicates, has been

46 suggested based on the compressibility of melt (Stixrude et al. 2009; Thomas et al. 2012; Muñoz

47 Ramo and Stixrude 2014) and partitioning of Fe into the liquid phase (Nomura et al. 2011;

48 Andrault et al. 2012). However, detailed characterization of mantle melt is challenging due to

49 experimental difficulties at deep mantle pressures. As low-temperature analogues of melts,

50 silicate glasses have been explored in recent high-pressure experiments (e.g. Nomura et al. 2011)

51 and computational studies (e.g. Stixrude and Karki 2005). In both silicate liquids and glasses a

52   range of coordination environments may evolve continuously with composition and pressure

53   (Stixrude and Karki 2005), but a surprising sharp transition was recently reported at ~70 GPa in

54   Fe-bearing melt and glass and attributed to an iron spin transition (Nomura et al. 2011).

55   Spin transitions in crystalline mantle phases and their implications for seismic properties

56   and chemical partitioning have been the focus of much recent study, particularly of ferropericlase

57   (Badro et al. 2003) and silicate perovskite (Badro et al. 2004). In ferropericlase, a spin transition

58   occurs in 6-fold-coordinated Fe^{2+} at pressures between 50 and 90 GPa, depending on Fe content

59   (Speziale et al. 2005; Fei et al. 2007). In silicate perovskite (now known as bridgmanite), the

60   presence of multiple sites and valence states makes characterizing the spin state more complex,

61   but both experiments and density functional theory results indicate that a spin transition occurs in

62   6-fold-coordinated Fe^{3+} at 15-50 GPa (Catalli et al. 2010; Hsu et al. 2011; Lin et al. 2012). At

63   high temperatures relevant to Earth's mantle, the effects of Maxwell-Boltzmann statistics and

64   kinetics have been predicted (Sturhahn et al. 2005; Tsuchiya et al. 2006; Lin and Tsuchiya 2008)

65   and observed (Lin et al. 2007; Kantor et al. 2009) to broaden each of these spin transitions to

66   occur over a pressure interval extending for ~30-50 GPa.

67   Liquids and glasses are characterized by continuous structural evolution under

68   compression that may also contribute to the pressure-broadening of spin transitions. At mantle

69   temperatures, the spin transition in liquid Fe_2SiO_4 has been predicted to take place over a >200

70   GPa pressure range (Muñoz Ramo and Stixrude 2014). While this transition might affect the

71   depth of a solid-liquid density crossover in the mantle, it would not be observable as a

72   discontinuity. In contrast, Nomura et al. (2011) reported a sharp change in Fe partitioning in

73   partially-melted $(Mg_{0.89}Fe_{0.11})_2SiO_4$ between 73 and 76 GPa. At similar pressures, between 59

74   and 77 GPa, they also observed that X-ray emission spectra of $(Mg_{0.95}Fe_{0.05})SiO_3$ glass indicated

75   a complete spin transition. Other studies are not consistent with abrupt spin transitions in liquids

76   and melts. No sharp change in partitioning was observed in chondritic melt at pressures up to 120

77   GPa (Andrault et al. 2012). Studies of several different Fe-bearing silicate glass compositions—

78   10-50% $FeSiO_3$, $Fe^{3+}/\Sigma Fe$ from 0-78%, with and without Al—showed either no change in spin

79   state (Mao et al. 2014; Prescher et al. 2014) or a gradual, partial change (Gu et al. 2012;

80   Murakami et al. 2014) at high pressures. Gradual increases in cation coordination rather than spin

81   transitions were inferred to be primarily responsible for pressure-induced changes in these glasses

82   (Mao et al. 2014; Prescher et al. 2014).

83   Studies of Fe spin state at extreme pressures rely on two complementary synchrotron

84   techniques: X-ray emission spectroscopy and Mössbauer spectroscopy. X-ray emission

85   spectroscopy (XES) measures energies of electron exchange between $3p$ and $3d$ orbitals, which

86   depend on bonding, coordination, valence and spin states (Peng et al. 1994; Rueff et al. 1999;

87   Mattila et al. 2007). This technique was the first used to identify pressure-induced spin transitions

88   in major lower mantle minerals (Badro et al. 2003, 2004). However, XES only provides a

89   constraint on the total spin moment of the bulk material, not of individual states or sites.

90   Mössbauer spectroscopy provides a complementary constraint on coordination, site occupancy,

91   valence, and spin states of Fe via the energies of recoil-free nuclear resonance in solid materials.

92   The technique can be applied to glasses but not silicate liquids; for insights on melt structures, a

93   wide variety of silicate glass compositions have been examined at ambient pressure by

94   Mössbauer spectroscopy (MS) with a conventional radioactive source (e.g. Mao et al. 1973;

95   Virgo and Mysen 1985; Jayasuriya et al. 2004; Dunlap and McGraw 2007; Rossano et al. 2007;

4

96   Cottrell and Kelley 2011). ^{57}Fe nuclei of each site, species and spin state resonate at energies with

97   isomer shift (IS), quadrupole splitting (QS) and hyperfine splitting that reflect the local electric

98   and magnetic fields. The relative intensities of each site indicate the abundance of Fe^{2+} and Fe^{3+}

99   in each spin state and coordination environment. For Mössbauer spectroscopy of materials at high

100   pressures, synchrotron radiation can provide a more brilliant, highly-focused source. Energy-

101   domain synchrotron Mössbauer spectroscopy (E-SMS) is identical to MS with the exception of a

102   more brilliant source obtained by monochromatizing a synchrotron beam to ~neV linewidth

103   (Smirnov et al. 1997; Mitsui et al. 2009; Potapkin et al. 2012). Mössbauer parameters IS and QS

104   can also be derived from nuclear forward scattering (also known as time-domain synchrotron

105   Mössbauer spectroscopy, T-SMS), in which nuclear resonance is observed in ~few hundred

106   nanosecond time windows between pulses of synchrotron radiation (Jackson et al. 2005;

107   Sturhahn et al. 2005). The combination of XES, E-SMS and T-SMS techniques offers an optimal

108   approach for separation of competing effects and thus understanding complex Fe-bearing

109   materials such as silicates at lower mantle conditions.

110   Fe,Al-bearing silicate glass compositions examined in previous studies are rich in ferric

111   iron; glass of almandine garnet composition provides a useful contrast as it is rich in both

112   aluminum and ferrous iron. Almandine is also of particular interest among silicate minerals for its

113   unusual electronic structure, with high quadrupole splitting at ambient conditions and at high

114   pressures (Dyar et al. 2006; Mao et al. 2013). At ~80 GPa and 2500 K, almandine end-member

115   $Fe_3Al_2Si_3O_{12}$ has been observed to transform to a single-phase orthorhombic perovskite

116   consistent with stoichiometry $(Fe_{0.75}Al_{0.25})(Al_{0.25}Si_{0.75})O_3$ (Dorfman et al. 2012). Structural

5

117 refinement of X-ray diffraction data for this phase shows that nearly all Fe resides in the larger A-

118 site and there are no discontinuities in its equation of state up to 150 GPa.

119   In this work, we apply multiple techniques to characterize the pressure-dependence of

120 valence and spin states in almandine glass at pressures up to 91 GPa. Total spin moment is

121 determined by XES. Valence, spin, and coordination states are constrained by E-SMS and T-

122 SMS.

123 ## 2. Material and methods

124   ^{57}Fe-enriched almandine glass was prepared from a stoichiometric mixture of ^{57}Fe$_2$O$_3$

125 (Cambridge Isotope Laboratories, Inc., ^{57}Fe 94.3%), Al$_2$O$_3$ (Alfa Aesar 99.9%) and SiO$_2$

126 (Johnson Matthey, 99.995%) after the method described by Geiger et al. (1987). Approximately

127 300 mg of reagents were placed in a covered graphite crucible and heated from 1000°C to

128 1200°C at a rate of 4°C/min. The sample was held at 1200°C for 6 minutes before being

129 quenched in air. To ensure a homogeneous product the resultant material was subsequently arc

130 melted under an argon atmosphere. The composition and homogeneity of the glass were

131 confirmed by microprobe analysis (Supplementary Table 1). The normalized formula,

132 Fe$_{2.69}$Al$_{2.14}$Si$_{2.93}$O$_{12}$, is slightly depleted in Fe and enriched in Al relative to pure almandine.

133   The valence state of Fe in the starting material was determined by Mössbauer

134 spectroscopy. MS was performed with a ^{57}Co radioactive source at the Advanced Photon Source

135 (APS) sector 3 offline Mössbauer laboratory. The spectrum was fit to a two-site model (Figure 1,

136 Table 1) using MossA software (Prescher et al. 2012). The dominant site, 82(3) percent of the

137 iron, has QS of 2.08(3) mm/s and IS relative to an iron standard of 0.982(14) mm/s. These

6

138 parameters are typical of Fe^{2+} in silicates (Dyar et al. 2006) and glasses (Dyar 1985; Virgo and

139 Mysen 1985; Burkhard 2000; Jayasuriya et al. 2004; Mysen 2006; Rossano et al. 2007; Gu et al.

140 2012; Mao et al. 2014; Murakami et al. 2014; Prescher et al. 2014). The QS of Fe^{2+} in almandine

141 glass is considerably lower than the 3.53 mm/s observed in crystalline almandine (Woodland and

142 Ross 1994; Dyar et al. 2006). A second site was observed with QS=1.23(11) mm/s and

143 IS=0.39(5) mm/s, consistent with Fe^{3+} in silicate glasses but with higher QS than Fe^{3+} in silicate

144 garnets. Our analysis yields $Fe^{3+}/\Sigma Fe$ of 18(3)%.

145   High-pressure experiments were performed using symmetric diamond anvil cells (DAC).

146 Glass samples were loaded with a ~8 μm ruby ball in NaCl, cryogenically-cooled Ar or

147 pressurized Ne (Rivers et al. 2008) (Figure 2). A 50- to 80-μm diameter hole was drilled through

148 a Re or Be gasket to serve as a sample chamber. Diamond anvils with 150-, 200- and 300-μm

149 culet size were used in separate experiments to reach maximum pressures of 91, 86, and 66 GPa,

150 respectively. Pressure was calibrated by ruby fluorescence (Mao et al. 1986) or Raman

151 spectroscopy of the tip of the diamond anvil (Akahama and Kawamura 2006).

152   XES was performed at pressures up to 66 GPa at beamline GALAXIES of Synchrotron

153 SOLEIL (Rueff et al. 2015). At GALAXIES, the beam size was 30x80 microns, incident energy

154 was 10 keV and typical count rates were 70-150 counts/s. The emission signal was maximized by

155 directing incident radiation through the diamond and collecting spectra at an angle of

156 approximately 10° minimizing the path through the beryllium gasket.

157   T-SMS experiments were conducted at pressures up to 85 GPa using beamline 16-ID-D of

158 the APS. Kirkpatrick-Baez mirrors were used to focus the X-ray beam to 30x40 μm. The storage

7

159   ring was operated in standard-mode with 24 bunches separated by 153 ns. Data were collected

160   between 14 and 130 ns after excitation. Measurements were taken both with and without a 0.5-

161   μm thick ^{57}Fe-enriched stainless steel foil as a reference. Sample count rates at high pressure

162   were 30-150 counts/s and spectra were typically collected for 30-60 minutes. At ambient

163   pressure, both T-SMS and MS give consistent results (Figure 1, Tables 1-2).

164   E-SMS experiments were conducted at pressures up to 91 GPa at beamline ID18 of the

165   European Synchrotron Radiation Facility (ESRF) (Rüffer and Chumakov 1996; Potapkin et al.

166   2012). The synchrotron beam was focused to 9x14 μm and monochromatized to a bandwidth of

167   ~5.5 neV at the ^{57}Fe resonant energy by a ^{57}FeBO$_3$ single crystal. The crystal monochromator

168   was oscillated in a sinusoidal mode over +/- 5 mm/s to provide a range of energies for absorption

169   measurements via the Doppler effect. Source velocity was calibrated with an α-Fe foil. The

170   linewidth and center shift of the source were verified before and after each measurement with

171   K$_2$Mg^{57}Fe(CN)$_6$ standard.

172   **3. Results**

173   Glass samples were compressed without heating to maximum pressures up to 91 GPa. At

174   ambient conditions, the glass is honey-brown and translucent, but darkens with pressure,

175   becoming black and opaque by 34 GPa (Figure 2). Pressure-induced color change of

176   (Mg$_{0.8}$Fe$_{0.2}$)SiO$_3$ enstatite-composition glass was determined by optical absorption spectroscopy

177   to occur from ~15-50 GPa (Murakami et al. 2014). An analogous color-change in crystalline

178   samples is known to be associated with the garnet-perovskite transition (O'Neill and Jeanloz

179   1994; Kesson et al. 1995; Dorfman et al. 2012) but is not observed in cold-compressed almandine

180 to pressures above 1 Mbar (Dorfman et al. 2012). This change in optical properties decreases

181 radiative thermal conductivity of Fe-bearing silicates in the mantle and may be associated with

182 changes in electronic configuration (Murakami et al. 2014).

183 **3. 1. X-ray emission spectroscopy**

184 The observed Fe Kβ X-ray emission spectrum at ambient conditions is composed of a

185 main $K\beta_{1,3}$ peak and a well-resolved lower-energy satellite Kβ' peak and is consistent with iron

186 entirely in the high spin state (Figure 3). Up to 66 GPa in almandine glass, the Kβ' peak intensity

187 continuously decreases and its breadth increases (Figure 3). These changes may be ascribed to

188 either a gradual spin-pairing transition or pressure-induced broadening effects (Gu et al. 2012;

189 Mao et al. 2014; Murakami et al. 2014).

190 Separating the effects of broadening and a spin transition requires quantitative comparison

191 with appropriate reference spectra. Several methods have been proposed for quantifying spin

192 crossovers (Kantor et al. 2006; Vankó et al. 2006; Mao et al. 2014) and each may lead to a

193 different interpretation of the data. Simple peak-fitting techniques do not adequately model the

194 Kβ spectrum due to the complexity of the energy multiplets from which the broader features are

195 composed (Vankó et al. 2006). Instead, the spin state is derived from an integrated difference

196 between spectra and reference high- and low-spin standard spectra. Identifying relevant standards

197 are keys to this method. Spectral differences can be due to differences in instrument resolution,

198 crystallographic environment, and stress conditions as well as spin state, so these confounding

199 factors must be minimized between the standards and experimental data (De Groot 2001; Vankó

200 et al. 2006; Mao et al. 2014). A modification of the integrated difference technique was recently

9

201   proposed to minimize the effects of pressure-induced broadening (Mao et al. 2014). Difference

202   spectra are summed such that negative differences at Kβ' are offset by positive differences in the

203   shoulder between Kβ' and Kβ$_{1,3}$. This integrated relative difference (IRD) method was suggested

204   to better model pressure-induced spin transitions both in (Mg,Fe)O ferropericlase and in Fe-

205   bearing silicate glass (Mao et al. 2014).

206   The IRD analysis was applied to the almandine glass XES using as references (Mg,Fe)O

207   from Lin et al. (2010) and the ambient-pressure glass spectrum. No significant difference is

208   observed between the glass at 1 bar and (Mg,Fe)O at 1 bar. IRD at high pressure relative to either

209   high-spin standard is identical within symbol size (Figure 3). Between 1 bar and the first high-

210   pressure measurement at 9 GPa, a decrease in total spin moment begins. Total spin moment

211   decreases gradually to ~80% of the high-spin standard by 27 GPa (Figure 3). At higher pressures

212   up to 66 GPa there is no significant further change in spin state. The further gradual changes in

213   the spectra above 27 GPa therefore reflect only broadening due to pressure gradients and/or

214   differential stress.

215   In previous work on silicate glass at high pressure, analysis by the integrated absolute

216   difference (IAD) method of Vankó et al. (2006) showed a gradual spin transition (Gu et al. 2012)

217   while the IRD method showed only broadening (Mao et al. 2014). Analysis of our spectra with

218   the IAD method also produces an apparent gradual loss of spin moment over the entire pressure

219   range (Supplementary Figure 1). We thus confirm that the IRD analysis removes pressure-

220   induced broadening and reduces the apparent change in spin relative to the IAD analysis, but we

221   still observe partial loss of spin moment. The spin change can be linked to a valence state and site

222   using Mössbauer spectroscopy.

10

223   **3. 2. Synchrotron Mössbauer spectroscopy**

224   Synchrotron Mössbauer spectroscopy was performed on almandine glass at high pressures

225   in both energy- and time-domain modes. E-SMS (Figure 4) and T-SMS spectra (Supplementary

226   Figure 2) evolve continuously with pressure. The major feature in E-SMS spectra is the

227   asymmetrical doublet identified as Fe^{2+}. With compression the Fe^{2+} doublet broadens and

228   becomes increasingly asymmetrical. Pressure-induced changes in the Fe^{2+} doublet are consistent

229   with previous E-SMS measurements of Fe^{2+}-rich glasses with compositions $(Mg_{0.8}Fe_{0.2})SiO_3$ and

230      $(Mg_{0.823}Fe_{0.135})(Al_{0.057}Si_{0.982})O_3$ (Murakami et al. 2014; Prescher et al. 2014). The small shoulder

231   observed between the Fe^{2+} lines (Figure 4) is identified as one leg of the Fe^{3+} doublet. At higher

232   pressures, a shoulder appears at higher velocity on the Fe^{2+} doublet.

233   T-SMS spectra (Supplementary Figure 2) at low pressure have a sharp beat at ~60 ns and

234   a broad decay after ~100 ns. At higher pressures, the beat shifts with pressure to faster times and

235   becomes less distinct. Above 26 GPa, another small beat appears at ~80 ns. Despite differences in

236      $Fe^{3+}/\Sigma Fe$ and total iron content, qualitatively similar spectra were observed at high pressure in

237      $(Mg_{0.80}Fe_{0.20})SiO_3$ (~10% Fe^{3+}) and $(Mg_{0.75}Fe_{0.20}Al_{0.10}Si_{0.95})O_3$ (~35% Fe^{3+}) glasses by Gu et al.

238   (2012) and $(Mg_{0.79}Fe_{0.10}Al_{0.10}Si_{0.96})O_3$ (78% Fe^{3+}) glass by Mao et al. (2014). However, resonant

239   intensity is also observed here at ~110 ns starting from 17 GPa which was not reported in the

240   earlier studies, possibly due to differences in composition, electronic states, or effective sample

241   thickness.

242   Modeling Mössbauer spectra of glasses is complicated by the range of coordination

243   environments and site geometries in the disordered structure. A simple two-site model with a

244   distribution over IS or QS cannot fit the asymmetry observed in E-SMS and the complex

11

245   structure in T-SMS. Due to the range of coordination environments, an asymmetrical

246   Fe^{2+} doublet is observed in silicate glasses (Mao et al. 1973; Alberto et al. 1996). At both ambient

247   conditions (Alberto et al. 1996; Lagarec and Rancourt 1997) and high pressures (Prescher et al.

248   2014), a correlated distribution over both IS and QS can fit the asymmetrical Fe^{2+} doublet

249   (Supplementary Figure 3). E-SMS data in this study were analyzed using the correlated

250   distribution model of Lagarec and Rancourt (1997) implemented for fitting E-SMS spectra in

251   MossA software (Prescher et al. 2012). The correlated distribution for Fe^{2+} can also be modeled

252   with a pair of doublets of approximately equal intensity, one representing low-IS, low-QS and the

253   other high-IS, high-QS (Supplementary Figure 3) (Virgo and Mysen 1985; Jayasuriya et al.

254   2004). T-SMS data in this study were analyzed using a paired Fe^{2+} doublet model with fixed

255   weighting in the CONUSS software package (Sturhahn 2000). T-SMS fits with a pair of doublets

256   for Fe^{2+} are consistent with observed E-SMS spectra (Supplementary Figure 2). Fe^{3+} doublets are

257   not fully resolved but assumed to be symmetric as previously observed at ambient pressure

258   (Virgo and Mysen 1985) and high pressure (Prescher et al. 2014).

259   Our results demonstrate consistent pressure-dependence of Mössbauer parameters in three

260   separate compression experiments with two SMS techniques (Figure 5, Tables 1-2). Observed

261   Mössbauer parameters for the Fe^{2+} doublet(s) at all conditions studied are consistent with

262   previous observations of high-spin Fe^{2+} in glasses (Dyar 1985; Virgo and Mysen 1985; Burkhard

263   2000), with average QS of 2.0-2.3 mm/s and IS of 0.8-1.1 mm/s. The QS of high-spin Fe^{2+}

264   increases slightly from 1 bar to 30 GPa and then slightly decreases up to the maximum pressure

265   of 91 GPa. The IS of high-spin Fe^{2+} decreases with pressure. The most significant change in the

266   Fe^{2+} component is an increase in the correlated broadening related to the covariance of QS and IS

12

267 particularly between 1 bar and ~40 GPa (Table 1). In T-SMS fits, the increase in correlated

268 broadening is modeled as a divergence of both QS and IS of two high-spin Fe^{2+} doublets. The

269 weight of the high-spin Fe^{2+} component does not change significantly. If the change in spin state

270 indicated by XES corresponds to a high-to-low spin transition in Fe^{2+}, we would expect a

271 decrease in QS of the Fe^{2+} site, as for the high-to-low spin transition in Fe^{2+} in bridgmanite (Hsu

272 et al. 2010), but this is not observed. Our data also do not support pressure-induced growth of an

273 intermediate spin Fe^{2+} component with parameters as reported by Murakami et al. (2014). The

274 broadening of the Fe^{2+} doublet could be interpreted as a gradual transition of half of the Fe^{2+}

275 component to intermediate spin below ~40 GPa. This is consistent with the total spin moment

276 measured by XES, but unlikely as there is no obvious reason why the spin transition would stop,

277 incomplete, at ~40 GPa.

278   Observations of the Fe^{3+} component(s) are consistent with a high-to-low spin transition.

279 At pressures >30 GPa, the values of QS for the Fe^{3+} site are 1.7-2.0 mm/s. These values are

280 outside the range of previous observations for high-spin Fe^{3+} at ambient conditions (Figures 5-6)

281 (Dyar 1985; Virgo and Mysen 1985; Burkhard 2000) and similar to previous observations of low-

282 spin Fe^{3+}-bearing compounds (Greenwood and Gibb 1971; Pasternak et al. 2002). Moreover, both

283 the weight of the Fe^{3+} component, ~20% of the total Fe, and the pressure at which the

284 Fe^{3+} shoulder completes its shift, ~30 GPa, match the decrease in spin moment observed in XES

285 data (Figure 3). A high-to-low spin transition in Fe^{3+} should be observed as a decrease in the

286 intensity of the high-spin doublet and corresponding growth of the low-spin doublet with lower

287 IS and higher QS (Pasternak et al. 2002). We have thus chosen a model with two Fe^{3+} doublets,

288 although these two doublets are not fully resolved in our MS data. We are also unable to resolve

13

289 the minimum pressure at which the low-spin Fe^{3+} appears, but at 15 GPa ~30% of the Fe^{3+} is in

290 the low-spin state. The high- and low-spin doublets coexist over a wider pressure range in the

291 glass sample loaded in NaCl vs. Ne medium. This suggests that differential stress may result in a

292 broader spin transition, as reported in (Mg,Fe)O (Lin et al. 2009).

293   Previous Mössbauer studies of silicate glasses found generally similar QS and IS values

294 and changes with pressure as in our study (Figure 6). QS and IS for all sites in the almandine

295 glass are similar to those constrained by previous E-SMS studies on Fe-bearing silicate glasses at

296 high pressures (Murakami et al. 2014; Prescher et al. 2014). Studies using both E-SMS and T-

297 SMS techniques on a wide range of compositions have found an increase in QS of Fe^{2+} at

298 pressures up to 20-40 GPa (Gu et al. 2012; Mao et al. 2014; Murakami et al. 2014; Prescher et al.

299 2014). A similar QS of high-pressure Fe^{3+} was observed in Fe^{3+}-rich glass studied by Prescher et

300 al. (2014) and Gu et al. (2012), but not by Mao et al. (2014). IS of Fe^{2+} was observed to decrease

301 with pressure in both previous E-SMS studies (Murakami et al. 2014; Prescher et al. 2014).

302 However, previous studies have offered different interpretations of these observations: no spin

303 transition (Mao et al. 2014; Prescher et al. 2014), a gradual high-to-low spin transition in

304 Fe^{3+} (Gu et al. 2012) or a high-to-intermediate spin transition in Fe^{2+} (Murakami et al. 2014). In

305 addition to differences in composition between these studies, differences in interpretation of

306 Mössbauer parameters are due to details of E-SMS and T-SMS fitting and availability and

307 interpretation of XES data.

308 ## 4. Discussion

14

309   The multiple techniques used in this study enable us to provide a strong constraint on the

310   pressure-dependence of spin states of Fe in almandine glass. Optical properties, XES, and

311   Mössbauer parameters of Fe^{3+} all exhibit changes between 1 bar and ~30 GPa. These results

312   support a gradual, complete transition of Fe^{3+} in almandine glass from high to low spin and no

313   detectable change in spin state of Fe^{2+}.

314   This transition in Fe^{3+} could not be reliably identified in previous studies that did not use

315   multiple experimental techniques. Fitting T-SMS spectra alone suffers from non-unique

316   constraints on Mössbauer parameters. Gu et al. (2012) model spectra using a pair of Fe^{2+} doublets

317   similar to those in this study, but their strong change in intensity with pressure is inconsistent

318   with other studies of silicate glasses and may be an artifact of non-unique fitting. Mao et al.

319   (2014) restrict their model to two sites of constant intensity, one each for high spin Fe^{2+} and Fe^{3+},

320   but their modeled energy-domain spectra exhibit varying degrees of asymmetry which is not

321   explained. The previous E-SMS study of Fe^{3+}-rich silicate glass (Prescher et al. 2014) finds a

322   similar increase in QS as in our observations of almandine glass (Figure 6). The doublet

323   identified at pressures above 20 GPa as intermediate spin Fe^{2+} by Murakami et al. (2014) is

324   consistent with Fe^{3+} at high pressures in this study and Prescher et al. (2014) (Figure 6).

325   However, previous studies using the E-SMS technique were not combined with XES

326   measurements and thus were unable to relate changes in Mössbauer parameters to changes in

327   total spin moment.

328   While our results and previous studies cover a wide range of compositions, all time- or

329   energy-domain Mössbauer studies of glass to date consistently find that there is no sharp

330   transition in spin or structure with pressure up to 126 GPa (Gu et al. 2012; Mao et al. 2014;

15

331 Murakami et al. 2014; Prescher et al. 2014). Almandine glass is much richer in Fe than the

332 compositions studied in other work; this may promote a spin transition at relatively lower

333 pressures (Prescher et al. 2014). The sharp spin transition observed in XES data by Nomura et al.

334 (2011) in $(Mg_{0.95}Fe_{0.05})SiO_3$ glass at 76 GPa is inconsistent with this study and others. Similar

335 experimental methods were used by Nomura et al. (2011) and more recent studies, and thus the

336 different results remain unexplained and unreplicated.

337   A spin transition in Fe^{3+} in silicate glasses is analogous to transitions in crystalline Fe-

338 bearing silicates. In bridgmanite, Fe^{3+} in the 6-fold-coordinated B-site is predicted theoretically to

339 undergo a spin transition at 40-70 GPa, but both Fe^{3+} and Fe^{2+} in the 8-fold-coordinated A-site

340 remain high-spin throughout the lower mantle pressure range (Hsu et al. 2010, 2011). Spin

341 transitions in Fe^{3+} have been observed at various pressures in the range of 13-70 GPa by several

342 experimental studies of bridgmanite (e.g. Catalli et al. 2010, 2011; Mao et al. 2011; Lin et al.

343 2012) and other Fe^{3+}-bearing perovskites (Xu et al. 2001; Pasternak et al. 2002; Rozenberg et al.

344 2005; Stan et al. 2015). In addition, a discontinuity in volumetric compression was attributed to a

345 spin transition in 6-fold-coordinated Fe^{3+} in andradite garnet at 60-70 GPa (Friedrich et al. 2014).

346 No spin transition has been observed in 8-fold-coordinated Fe^{2+} in pyrope-almandine garnets, but

347 studies of the equation of state and electronic configuration of these garnets have only reached

348 ~30 GPa (e.g. Mao et al. 2013).

349   In silicate glass, Fe^{3+} and Fe^{2+} both occupy a range of coordination environments. In

350 $MgSiO_3$ glasses, the average coordination number is 6 in the Mg-site and 4 in the Si-site, and

351 these averages increase with pressure (Funamori et al. 2004). The average coordination of Si in

352 SiO_2 glass has been suggested by experiments and simulations to increase stepwise or

16

353 continuously with compression (e.g. Meade et al. 1992). While compression alone generally

354 increases QS while decreasing IS (e.g. Pasternak et al. 2002; Kantor et al. 2006), increasing

355 coordination of Fe increases both QS and IS (Dyar et al. 2006). Observed increases in QS of Fe^{2+}

356 with pressure in silicate glasses have been interpreted to show densification by increasing

357 coordination number to 8-12 (Mao et al. 2014). However, in the almandine glass we observe not

358 only a slight increase in QS but an increase in broadening of the Fe^{2+} site. This doublet represents

359 a superposition of multiple sites with different coordination which cannot be resolved in the

360 glass. Pressure-induced changes in Mössbauer parameters of Fe^{2+} do not depend on pressure

361 medium and are thus unlikely to be due to non-hydrostatic stress. The increase in correlated

362 broadening of the Fe^{2+} doublet with compression (Figure 7) suggests development of a wider

363 range of coordination environments. The population of Fe^{2+} with highest QS and IS, in higher

364 coordination, would thus increase with pressure without completely replacing Fe^{2+} with lowest

365 QS and IS, in lower coordination.

5. Implications

367   A sharp spin transition in iron in silicate glasses would suggest a discontinuity in the

368 properties of melt in the lower mantle or deep in a magma ocean; conversely, a continuous spin

369 transition supports a smooth variation of the properties of silicate melts with depth. This study

370 represents the first high-pressure examination of almandine glass and the first combination of

371 energy- and time-domain synchrotron Mössbauer spectra and X-ray emission spectra techniques

372 at high pressure for any silicate glass. All methods consistently support a broad spin transition in

373 Fe^{3+} between 1 bar and ~30 GPa without an abrupt discontinuity. Our observations differ from

17

374   the previous observation of a sharp transition in Fe-bearing glass and accompanying changes in

375   solid-melt iron partitioning. We would expect that in a melt of almandine composition, effects of

376   temperature may further broaden the spin transition to a greater range than the ~30-GPa interval

377   observed in the glass. Our study supports the expectation that spin transitions in iron-bearing

378   silicate melts in Earth's mantle should be broad with respect to transitions in their crystalline

379   counterparts. No discontinuities are expected to occur under compression in the density or

380   transport properties of Fe-rich mantle melts.

381   In addition, the bonding of Fe^{2+} shifts to a broader range of coordination numbers over 1

382   bar to ~60 GPa. These changes are accompanied by a change in color from transparent to black,

383   suggesting a pressure-induced reduction in radiative thermal conductivity in Fe-rich silicate

384   liquids. This increasing diversity of bonding styles may have important implications for transport

385   properties of the glass or melt network in the Earth's deep mantle or early magma ocean.

References

408 Akahama, Y., and Kawamura, H. (2006) Pressure calibration of diamond anvil Raman gauge to
409   310 GPa. Journal of Applied Physics, 100, 043516–4.

410 Alberto, H.V., Pinto da Cunha, J.L., Mysen, B.O., Gil, J.M., and Ayres de Campos, N. (1996)
411   Analysis of Mössbauer spectra of silicate glasses using a two-dimensional Gaussian
412   distribution of hyperfine parameters. Journal of Non-Crystalline Solids, 194, 48–57.

413 Andrault, D., Petitgirard, S., Nigro, G.L., Devidal, J.-L., Veronesi, G., Garbarino, G., and
414   Mezouar, M. (2012) Solid-liquid iron partitioning in Earth's deep mantle. Nature, 487,
415   354–357.

416 Badro, J., Fiquet, G., Guyot, F., Rueff, J.-P., Struzhkin, V.V., Vankó, G., and Monaco, G. (2003)
417   Iron Partitioning in Earth's Mantle: Toward a Deep Lower Mantle Discontinuity. Science,
418   300, 789–791.

19

419   Badro, J., Rueff, J.-P., Vanko, G., Monaco, G., Fiquet, G., and Guyot, F. (2004) Electronic
420   Transitions in Perovskite: Possible Nonconvecting Layers in the Lower Mantle. Science,
421   305, 383–386.

422   Burkhard, D.J.M. (2000) Iron-bearing silicate glasses at ambient conditions. Journal of Non-
423   Crystalline Solids, 275, 175–188.

424   Catalli, K., Shim, S.-H., Prakapenka, V.B., Zhao, J., Sturhahn, W., Chow, P., Xiao, Y., Liu, H.,
425   Cynn, H., and Evans, W.J. (2010) Spin state of ferric iron in $MgSiO_3$ perovskite and its
426   effect on elastic properties. Earth and Planetary Science Letters, 289, 68–75.

427   Catalli, K., Shim, S.-H., Dera, P., Prakapenka, V.B., Zhao, J., Sturhahn, W., Chow, P., Xiao, Y.,
428   Cynn, H., and Evans, W.J. (2011) Effects of the Fe^{3+} spin transition on the properties of
429   aluminous perovskite—New insights for lower-mantle seismic heterogeneities. Earth and
430   Planetary Science Letters, 310, 293–302.

431   Cottrell, E., and Kelley, K.A. (2011) The oxidation state of Fe in MORB glasses and the oxygen
432   fugacity of the upper mantle. Earth and Planetary Science Letters, 305, 270–282.

433   De Groot, F. (2001) High-resolution X-ray emission and X-ray absorption spectroscopy.
434   Chemical Reviews, 101, 1779–1808.

435   Dorfman, S.M., Shieh, S.R., Meng, Y., Prakapenka, V.B., and Duffy, T.S. (2012) Synthesis and
436   equation of state of perovskites in the $(Mg, Fe)_3Al_2Si_3O_{12}$ system to 177 GPa. Earth and
437   Planetary Science Letters, 357–358, 194–202.

438   Dunlap, R.A., and McGraw, J.D. (2007) A Mössbauer effect study of Fe environments in impact
439   glasses. Journal of Non-Crystalline Solids, 353, 2201–2205.

440   Dyar, M.D. (1985) A review of Moessbauer data on inorganic glasses; the effects of composition
441   on iron valency and coordination. American Mineralogist, 70, 304–316.

442   Dyar, M.D., Agresti, D.G., Schaefer, M.W., Grant, C.A., and Sklute, E.C. (2006) Mössbauer
443   spectroscopy of Earth and planetary materials. Annual Review of Earth and Planetary
444   Sciences, 34, 83–125.

445   Fei, Y., Zhang, L., Corgne, A., Watson, H., Ricolleau, A., Meng, Y., and Prakapenka, V. (2007)
446   Spin transition and equations of state of (Mg, Fe)O solid solutions. Geophysical Research
447   Letters, 34, L17307.

448   Friedrich, A., Winkler, B., Morgenroth, W., Ruiz-Fuertes, J., Koch-Müller, M., Rhede, D., and
449   Milman, V. (2014) Pressure-induced spin collapse of octahedrally coordinated Fe^{3+} in
450        $Ca_3Fe_2[SiO_4]_3$ from experiment and theory. Physical Review B, 90, 094105.

451   Funamori, N., Yamamoto, S., Yagi, T., and Kikegawa, T. (2004) Exploratory studies of silicate
452   melt structure at high pressures and temperatures by in situ X-ray diffraction. Journal of
453   Geophysical Research: Solid Earth, 109, B03203.

454   Geiger, C.., Newton, R.., and Kleppa, O.. (1987) Enthalpy of mixing of synthetic almandine-
455   grossular and almandine-pyrope garnets from high-temperature solution calorimetry.
456   Geochimica et Cosmochimica Acta, 51, 1755–1763.

457   Greenwood, N.N., and Gibb, T.C. (1971) Low-spin Iron(II) and Iron(III) Complexes. In
458   Mössbauer Spectroscopy pp. 169–193. Springer Netherlands.

459   Gu, C., Catalli, K., Grocholski, B., Gao, L., Alp, E., Chow, P., Xiao, Y., Cynn, H., Evans, W.J.,
460   and Shim, S.-H. (2012) Electronic structure of iron in magnesium silicate glasses at high
461   pressure. Geophysical Research Letters, 39.

462   Hsu, H., Umemoto, K., Blaha, P., and Wentzcovitch, R.M. (2010) Spin states and hyperfine
463   interactions of iron in $(Mg,Fe)SiO_3$ perovskite under pressure. Earth and Planetary
464   Science Letters, 294, 19–26.

465   Hsu, H., Blaha, P., Cococcioni, M., and Wentzcovitch, R.M. (2011) Spin-State Crossover and
466   Hyperfine Interactions of Ferric Iron in $MgSiO_3$ Perovskite. Physical Review Letters, 106,
467   118501.

468   Jackson, J.M., Sturhahn, W., Shen, G., Zhao, J., Hu, M.Y., Errandonea, D., Bass, J.D., and Fei,
469   Y. (2005) A synchrotron Mössbauer spectroscopy study of $(Mg,Fe)SiO_3$ perovskite up to
470   120 GPa. American Mineralogist, 90, 199–205.

471   Jayasuriya, K.D., O'Neill, H.S.C., Berry, A.J., and Campbell, S.J. (2004) A Mössbauer study of
472   the oxidation state of Fe in silicate melts. American Mineralogist, 89, 1597–1609.

473   Kantor, I., Dubrovinsky, L., McCammon, C., Steinle-Neumann, G., Kantor, A., Skorodumova,
474   N., Pascarelli, S., and Aquilanti, G. (2009) Short-range order and Fe clustering in
475         $Mg_{1−x}Fe_xO$ under high pressure. Physical Review B, 80, 014204.

476   Kantor, I.Y., Dubrovinsky, L.S., and McCammon, C.A. (2006) Spin crossover in (Mg,Fe)O: A
477   Mössbauer effect study with an alternative interpretation of x-ray emission spectroscopy
478   data. Physical Review B, 73, 100101.

479   Kesson, S.E., Fitzgerald, J.D., Shelley, J.M.G., and Withers, R.L. (1995) Phase relations,
480   structure and crystal chemistry of some aluminous silicate perovskites. Earth and
481   Planetary Science Letters, 134, 187–201.

482   Labrosse, S., Hernlund, J.W., and Coltice, N. (2007) A crystallizing dense magma ocean at the
483   base of the Earth's mantle. Nature, 450, 866–869.

21

484   Lagarec, K., and Rancourt, D.G. (1997) Extended Voigt-based analytic lineshape method for
485   determining N-dimensional correlated hyperfine parameter distributions in Mössbauer
486   spectroscopy. Nuclear Instruments and Methods in Physics Research Section B: Beam
487   Interactions with Materials and Atoms, 129, 266–280.

488   Lee, C. -t. A., Luffi, P., Hoink, T., Li, J., Dasgupta, R., and Hernlund, J. (2010) Upside-down
489   differentiation and generation of a "primordial" lower mantle. Nature, 463, 930–933.

490   Lin, J.-F., and Tsuchiya, T. (2008) Spin transition of iron in the Earth's lower mantle. Physics of
491   the Earth and Planetary Interiors, 170, 248–259.

492   Lin, J.-F., Vankó, G., Jacobsen, S.D., Iota, V., Struzhkin, V.V., Prakapenka, V.B., Kuznetsov, A.,
493   and Yoo, C.-S. (2007) Spin Transition Zone in Earth's Lower Mantle. Science, 317, 1740
494   –1743.

495   Lin, J.-F., Wenk, H.-R., Voltolini, M., Speziale, S., Shu, J., and Duffy, T.S. (2009) Deformation
496   of lower-mantle ferropericlase (Mg,Fe)O across the electronic spin transition. Physics and
497   Chemistry of Minerals, 36, 585–592.

498   Lin, J.-F., Mao, Z., Jarrige, I., Xiao, Y., Chow, P., Okuchi, T., Hiraoka, N., and Jacobsen, S.D.
499   (2010) Resonant X-ray emission study of the lower-mantle ferropericlase at high
500   pressures. American Mineralogist, 95, 1125–1131.

501   Lin, J.-F., Alp, E.E., Mao, Z., Inoue, T., McCammon, C., Xiao, Y., Chow, P., and Zhao, J. (2012)
502   Electronic spin states of ferric and ferrous iron in the lower-mantle silicate perovskite.
503   American Mineralogist, 97, 592–597.

504   Mao, H.K., Virgo, D., and Bell, P.M. (1973) Analytical Study of the Orange Lunar Soil Returned
505   by the Apollo 17 Astronauts. In Year Book Carnegie Institution of Washington pp. 631–
506   638. Carnegie Institution of Washington, Washington, D.C.

507   Mao, H. -k., Xu, J., and Bell, P.M. (1986) Calibration of the Ruby Pressure Gauge to 800 kbar
508   Under Quasi-Hydrostatic Conditions. Journal of Geophysical Research, 91, 4673–4676.

509   Mao, Z., Lin, J.F., Scott, H.P., Watson, H.C., Prakapenka, V.B., Xiao, Y., Chow, P., and
510   McCammon, C. (2011) Iron-rich perovskite in the Earth's lower mantle. Earth and
511   Planetary Science Letters, 309, 179–184.

512   Mao, Z., Lin, J.-F., Huang, S., Chen, J., Xiao, Y., and Chow, P. (2013) Synchrotron Mössbauer
513   study of Fe-bearing pyrope at high pressures and temperatures. American Mineralogist,
514   98, 1146–1152.

515   Mao, Z., Lin, J.-F., Yang, J., Wu, J., Watson, H.C., Xiao, Y., Chow, P., and Zhao, J. (2014) Spin
516   and valence states of iron in Al-bearing silicate glass at high pressures studied by
517   synchrotron Mössbauer and X-ray emission spectroscopy. American Mineralogist, 99,
518   415–423.

22

519 Mattila, A., Rueff, J.-P., Badro, J., Vankó, G., and Shukla, A. (2007) Metal-ligand interplay in
520   strongly correlated oxides: A parametrized phase diagram for pressure-induced spin
521   transitions. Physical Review Letters, 98, 196404.

522 Meade, C., Hemley, R.J., and Mao, H.K. (1992) High-pressure x-ray diffraction of SiO_2 glass.
523   Physical Review Letters, 69, 1387–1390.

524 Mitsui, T., Hirao, N., Ohishi, Y., Masuda, R., Nakamura, Y., Enoki, H., Sakaki, K., and Seto, M.
525   (2009) Development of an energy-domain ^{57}Fe-Mössbauer spectrometer using
526   synchrotron radiation and its application to ultrahigh-pressure studies with a diamond
527   anvil cell. Journal of Synchrotron Radiation, 16, 723–729.

528 Muñoz Ramo, D., and Stixrude, L. (2014) Spin crossover in Fe_2SiO_4 liquid at high pressure.
529   Geophysical Research Letters, 41.

530 Murakami, M., Goncharov, A.F., Hirao, N., Masuda, R., Mitsui, T., Thomas, S.-M., and Bina,
531   C.R. (2014) High-pressure radiative conductivity of dense silicate glasses with potential
532   implications for dark magmas. Nature Communications, 5.

533 Mysen, B.O. (2006) The structural behavior of ferric and ferrous iron in aluminosilicate glass
534   near meta-aluminosilicate joins. Geochimica et Cosmochimica Acta, 70, 2337–2353.

535 Nomura, R., Ozawa, H., Tateno, S., Hirose, K., Hernlund, J., Muto, S., Ishii, H., and Hiraoka, N.
536   (2011) Spin crossover and iron-rich silicate melt in the Earth's deep mantle. Nature, 473,
537   199–202.

538 O'Neill, B., and Jeanloz, R. (1994) $MgSiO_3$-$FeSiO_3$-Al_2O_3 in the Earth's lower mantle:
539   Perovskite and garnet at 1200 km depth. Journal of Geophysical Research, 99, 19,901–
540   19,915.

541 Pasternak, M.P., Xu, W.M., Rozenberg, G.K., and Taylor, R.D. (2002) Electronic, Magnetic and
542   Structural Properties of the $RFeO_3$ Antiferromagnetic-Perovskites at Very High Pressures.
543   In Symposium D – Perovskite Materials Vol. 718.

544 Peng, G., Wang, X., Randall, C.R., Moore, J.A., and Cramer, S.P. (1994) Spin selective x-ray
545   absorption spectroscopy: Demonstration using high resolution Fe Kβ fluorescence.
546   Applied Physics Letters, 65, 2527–2529.

547 Potapkin, V., Chumakov, A.I., Smirnov, G.V., Celse, J.-P., Rüffer, R., McCammon, C., and
548   Dubrovinsky, L. (2012) The ^{57}Fe Synchrotron Mössbauer Source at the ESRF. Journal of
549   Synchrotron Radiation, 19, 559–569.

550 Prescher, C., McCammon, C., and Dubrovinsky, L. (2012) MossA: a program for analyzing
551   energy-domain Mössbauer spectra from conventional and synchrotron sources. Journal of
552   Applied Crystallography, 45, 329–331.

553 Prescher, C., Weigel, C., McCammon, C., Narygina, O., Potapkin, V., Kupenko, I., Sinmyo, R.,
554   Chumakov, A.I., and Dubrovinsky, L. (2014) Iron spin state in silicate glass at high
555   pressure: Implications for melts in the Earth s lower mantle. Earth and Planetary Science
556   Letters, 385, 130–136.

557 Rivers, M., Prakapenka, V., Kubo, A., Pullins, C., Holl, C.M., and Jacobsen, S.D. (2008) The
558   COMPRES/GSECARS gas-loading system for diamond anvil cells at the Advanced
559   Photon Source. High Pressure Research, 28, 273–292.

560 Rossano, S., Behrens, H., and Wilke, M. (2007) Advanced analyses of ^{57}Fe Mössbauer data of
561   alumino-silicate glasses. Physics and Chemistry of Minerals, 35, 77–93.

562 Rozenberg, G.K., Pasternak, M.P., Xu, W.M., Dubrovinsky, L.S., Carlson, S., and Taylor, R.D.
563   (2005) Consequences of pressure-instigated spin crossover in $RFeO_3$ perovskites; a
564   volume collapse with no symmetry modification. EPL (Europhysics Letters), 71, 228.

565 Rueff, J.-P., Kao, C.-C., Struzhkin, V.V., Badro, J., Shu, J., Hemley, R.J., and Mao, H.K. (1999)
566   Pressure-Induced High-Spin to Low-Spin Transition in FeS Evidenced by X-Ray
567   Emission Spectroscopy. Physical Review Letters, 82, 3284.

568 Rueff, J.-P., Ablett, J.M., Céolin, D., Prieur, D., Moreno, T., Balédent, V., Lassalle-Kaiser, B.,
569   Rault, J.E., Simon, M., and Shukla, A. (2015) The GALAXIES beamline at the SOLEIL
570   synchrotron: inelastic X-ray scattering and photoelectron spectroscopy in the hard X-ray
571   range. Journal of Synchrotron Radiation, 22.

572 Rüffer, R., and Chumakov, A.I. (1996) Nuclear Resonance Beamline at ESRF. Hyperfine
573   Interactions, 97-98, 589–604.

574 Smirnov, G.V., van Bürck, U., Chumakov, A.I., Baron, A.Q.R., and Rüffer, R. (1997)
575   Synchrotron Mössbauer source. Physical Review B, 55, 5811–5815.

576 Speziale, S., Milner, A., Lee, V.E., Clark, S.M., Pasternak, M.P., and Jeanloz, R. (2005) Iron spin
577   transition in Earth's mantle. Proceedings of the National Academy of Sciences of the
578   United States of America, 102, 17918–17922.

579 Stan, C.V., Wang, J., Zouboulis, I.S., Prakapenka, V., and Duffy, T.S. (2015) High-pressure
580   phase transition in $Y_3Fe_5O_{12}$. Journal of Physics: Condensed Matter, 27, 405401.

581 Stixrude, L., and Karki, B. (2005) Structure and Freezing of $MgSiO_3$ Liquid in Earth's Lower
582   Mantle. Science, 310, 297–299.

583 Stixrude, L., de Koker, N., Sun, N., Mookherjee, M., and Karki, B.B. (2009) Thermodynamics of
584   silicate liquids in the deep Earth. Earth and Planetary Science Letters, 278, 226–232.

585 Sturhahn, W. (2000) CONUSS and PHOENIX: Evaluation of nuclear resonant scattering data.
586   Hyperfine Interactions, 125, 149–172.

587   Sturhahn, W., Jackson, J.M., and Lin, J.-F. (2005) The spin state of iron in minerals of Earth's
588   lower mantle. Geophysical Research Letters, 32, L12307.

589   Thomas, C.W., Liu, Q., Agee, C.B., Asimow, P.D., and Lange, R.A. (2012) Multi-technique
590   equation of state for Fe_2SiO_4 melt and the density of Fe-bearing silicate melts from 0 to
591   161 GPa. Journal of Geophysical Research: Solid Earth, 117, B10206.

592   Tsuchiya, T., Wentzcovitch, R.M., da Silva, C.R., and de Gironcoli, S. (2006) Spin transition in
593   magnesiowüstite in Earth's lower mantle. Physical Review Letters, 96, 198501.

594   Vankó, G., Neisius, T., Molnár, G., Renz, F., Karpati, S., Shukla, A., and de Groot, F.M.F.
595   (2006) Probing the 3d spin momentum with X-ray emission spectroscopy: The case of
596   molecular-spin transitions. The Journal of Physical Chemistry B, 110, 11647–11653.

597   Virgo, D., and Mysen, B.O. (1985) The structural state of iron in oxidized vs. reduced glasses at
598   1 atm: A ^{57}Fe Mössbauer study. Physics and Chemistry of Minerals, 12, 65–76.

599   Williams, Q., and Garnero, E.J. (1996) Seismic Evidence for Partial Melt at the Base of Earth's
600   Mantle. Science, 273, 1528–1530.

601   Woodland, A.B., and Ross, C.R. (1994) A crystallographic and Mössbauer spectroscopy study of
602         $Fe_3^{2+}Al_2Si_3O_{12}$-$Fe_3^{2+}Fe_2^{3+}Si_3O_{12}$,   (almandine-"skiagite")   and $Ca_3Fe_2^{3+}Si_3O_{12}$-
603         $Fe_3^{2+}Fe_2^{3+}Si_3O_{12}$ (andradite-"skiagite") garnet solid solutions. Physics and Chemistry of
604   Minerals, 21, 117–132.

605   Xu, W.M., Naaman, O., Rozenberg, G.K., Pasternak, M.P., and Taylor, R.D. (2001) Pressure-
606   induced breakdown of a correlated system: The progressive collapse of the Mott-
607   Hubbard state in $RFeO_3$. Physical Review B, 64, 094411.

608

609

610 **List of figure captions**

611 Table 1: Mössbauer parameters observed by energy-domain Mössbauer spectroscopy for glass

612 compressed in Ne or NaCl medium. QS=quadrupole splitting, IS=isomer shift, ρ=covariance of

613 distributions of QS and IS, FWHM=line full width at half maximum.

614 Table 2: Mössbauer parameters observed by time-domain Mössbauer spectroscopy for glass

615 compressed in Ne medium. QS=quadrupole splitting, ΔIS=difference in isomer shift between

616 Fe^{2+} and Fe^{3+} doublets, FWHM=full width at half maximum. ΔIS is given due to limited absolute

617 reference constraint on IS. Starred parameters were fixed in fits. Fitting uncertainties for QS and

618 IS are ~0.01 mm/s.

619 Figure 1: a) Conventional (energy-domain) and b) synchrotron Mössbauer (time-domain) spectra

620 of almandine glass at 1 bar and 2-site fit (solid line). Residual for energy-domain fit is shown by

621 gray dots in the upper part of the figure. Fe^{2+} and Fe^{3+} doublets are shown in dark and light gray,

622 respectively.

623 Figure 2: Photomicrograph of opaque, black glass sample at 34 GPa in Ne medium with ruby

624 ball.

625 Figure 3: XES spectra for almandine glass normalized to area and shifted to position of the main

626 peak (Mao et al. 2014). Difference spectra below are relative to the low-spin (Mg,Fe)O reference

627 (Lin et al. 2010). Inset: total spin moment calculated from XES spectra (black) and from weight

628 of low-spin Fe^{3+} component in E-SMS spectra (red). TSM for XES was determined from the

26

629   integrated relative difference (IRD) between spectra and high- and low-spin (Mg,Fe)O references

630   (Lin et al. 2010).

631   Figure 4: Energy-domain synchrotron Mössbauer spectra for almandine glass in a neon pressure

632   medium. Data are displayed as open circles. Curves are high-spin Fe^{2+} doublet fit (blue), high-

633   spin Fe^{3+} doublet fit (pink), low-spin Fe^{3+} doublet fit (red), baseline (gray) and total fit (black).

634   Figure 5: Observed Mössbauer parameters from almandine glass. Fe^{2+} component is represented

635   by two doublets in time-domain measurements (open symbols) and a single doublet with

636   correlated quadrupole splitting and isomer shift in energy-domain measurements (filled symbols).

637   Separate high- and low-spin Fe^{3+} components are modeled in energy-domain measurements. a)

638   Quadrupole splitting of each doublet. Triangles joined by lines represent the two Fe^{2+} sites used

639   to model the range of Fe^{2+} environments in time-domain fits. b) Weight of each doublet. Two

640   Fe^{2+} doublets of equal weight are used for time-domain fits.

641   Figure 6: Quadrupole splitting vs. isomer shift for silicate and inorganic glasses derived from

642   energy-domain Mössbauer spectroscopy. Literature values for glasses at ambient conditions are

643   shown in small open black squares (Dyar 1985; Virgo and Mysen 1985; Burkhard 2000). Colors

644   indicate Fe species identified at high pressure: dark blue=high-spin Fe^{2+}, light blue = intermediate

645   spin Fe^{2+}, pink=high-spin Fe^{3+}, red= low-spin Fe^{3+}. Glasses at high pressures are shown with

646   filled symbols (triangles=Prescher et al. (2014), diamonds=Murakami et al. (2014), circles= this

647   study). Arrows indicate change observed with increasing pressure.

648   Figure 7: Correlation parameter of distribution of QS and IS in fits of Fe^{2+} doublet. Solid

649   symbols: compression in Ne medium. Open symbols: compression in NaCl medium.

650   27

651   **Table 1**

	High spin Fe^{2+}			
Pressure (GPa)	Weight (%)	QS (mm/s)	IS (mm/s)	ρ
Ambient				
0.0001	82(3)	2.08(3)	0.982(14)	0.273
Ne medium				
0.2	81(12)	1.99(2)	1.089(10)	0.525
5	87(4)	2.07(2)	1.086(12)	0.423
15	87(4)	2.247(19)	1.035(13)	0.557
41	88(4)	2.24(2)	0.959(10)	0.765
54	89(5)	2.18(4)	0.890(14)	0.826
NaCl medium				
7	87.6(1.9)	2.05(2)	1.066(9)	0.339
18	84(3)	2.319(14)	1.036(12)	0.491
30	85(5)	2.30(3)	0.99(2)	0.682
42	84(5)	2.26(3)	0.94(2)	0.785
57	86(6)	2.20(4)	0.86(3)	0.773
70	84(6)	2.13(4)	0.86(4)	0.967
91	86(5)	2.05(3)	0.81(3)	0.859

	High spin Fe^{3+}				Low spin Fe^{3+}			
Pressure (GPa)	Weight (%)	QS (mm/s)	IS (mm/s)	FWHM (mm/s)	Weight (%)	QS (mm/s)	IS (mm/s)	FWHM (mm/s)
Ambient								
0.0001	18(3)	1.23(11)	0.39(5)	0.63(13)				
Ne medium								
0.2	19(8)	1.18(9)	0.43(5)	0.58(12)	--	--	--	--
5	13(6)	1.20(18)	0.46(10)	0.53(15)	--	--	--	--
15	9(3)	0.74(13)	0.57(5)	0.36(16)	4(4)	1.74(10)	0.48(5)	0.2(2)
41	--	--	--	--	12(4)	1.82(7)	0.36(3)	0.33(10)
54	--	--	--	--	11(4)	1.83(6)	0.35(3)	0.36(13)
NaCl medium								
7	12.4(1.9)	1.17(13)	0.41(7)	0.50(12)	--	--	--	--
18	9.1(1.7)	0.90(7)	0.64(3)	0.32(7)	7(3)	1.97(5)	0.53(3)	0.23(10)
30	5(3)	0.90(8)	0.61(4)	0.25(12)	9(5)	1.88(7)	0.42(3)	0.31(13)
42	4(3)	0.92(8)	0.62(3)	0.24(13)	12(5)	1.93(7)	0.41(3)	0.35(11)
57	4(3)	0.99(7)	0.62(3)	0.20(14)	10(5)	2.00(7)	0.38(3)	0.33(12)
70	--	--	--	--	16(6)	1.88(6)	0.34(3)	0.39(11)
91	--	--	--	--	14(5)	1.84(6)	0.30(3)	0.40(11)

652

653

28

654   **Table 2**

Fe^{2+}								
Pressure (GPa)	Weight (%)	QS (mm/s)	ΔIS (mm/s)	FWHM (mm/s)	Weight (%)	QS (mm/s)	ΔIS (mm/s)	FWHM (mm/s)
0.0001	83	2.10	0.56	0.63				
6	40*	1.90	0.55	0.68	40*	2.25	0.66	0.79
17	40*	2.07	0.55	0.70	40*	2.34	0.83	0.74
26	40*	1.99	0.57	0.69	40*	2.64	0.69	0.75
37	40*	2.02	0.54	0.71	40*	2.66	0.75	0.76
47	40*	1.95	0.54	0.72	40*	2.67	0.77	0.74
56	40*	2.02	0.51	0.71	40*	2.66	0.78	0.77
65	40*	2.01	0.50	0.69*	40*	2.66	0.79	0.78*
76	40*	1.91	0.51	0.69	40*	2.66	0.77	0.78
85	40*	1.88	0.54	0.69*	40*	2.66	0.80	0.78*

Fe^{3+}			
Pressure (GPa)	Weight (%)	QS (mm/s)	FWHM (mm/s)
0.0001	17	1.17	0.77
6	20*	1.14	0.64
17	20*	1.58	0.63
26	20*	1.72	0.59
37	20*	1.81	0.54
47	20*	1.81	0.53
56	20*	1.84	0.51
65	20*	1.83	0.48*
76	20*	1.77	0.48
85	20*	1.77	0.48*

655

656

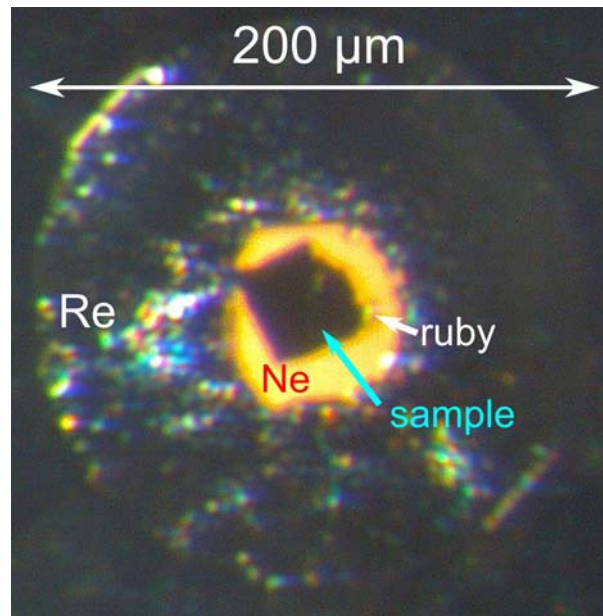657

29

658   **Figures**
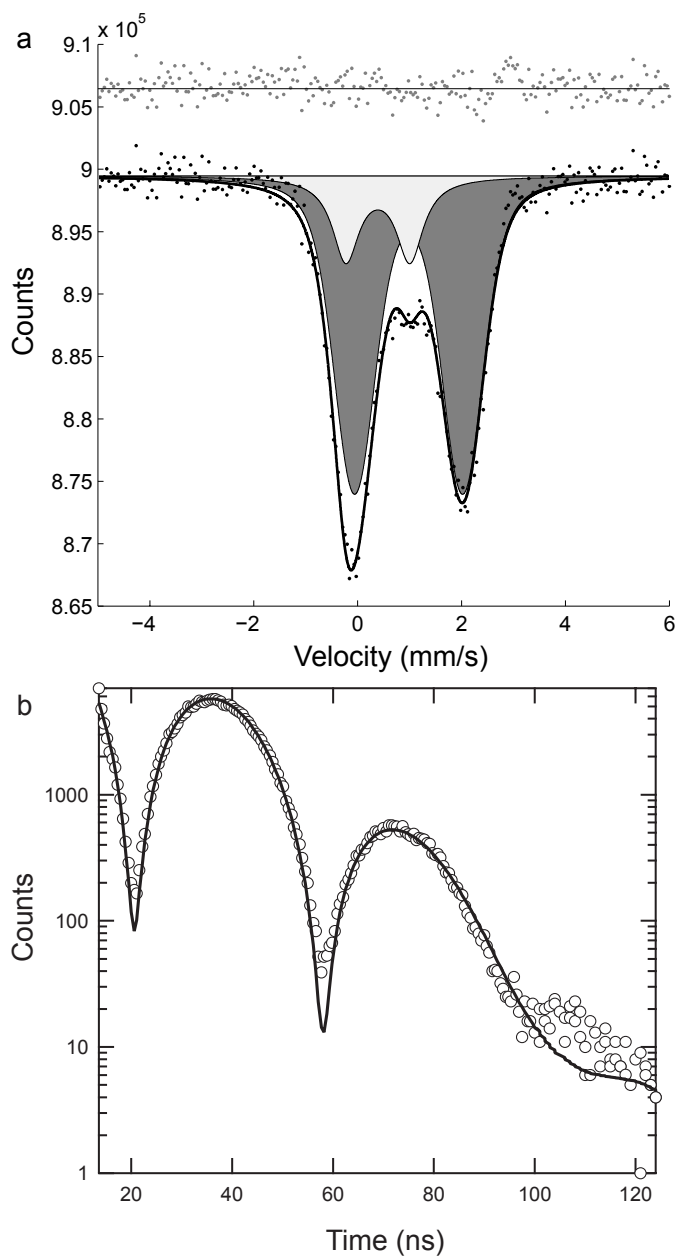
659
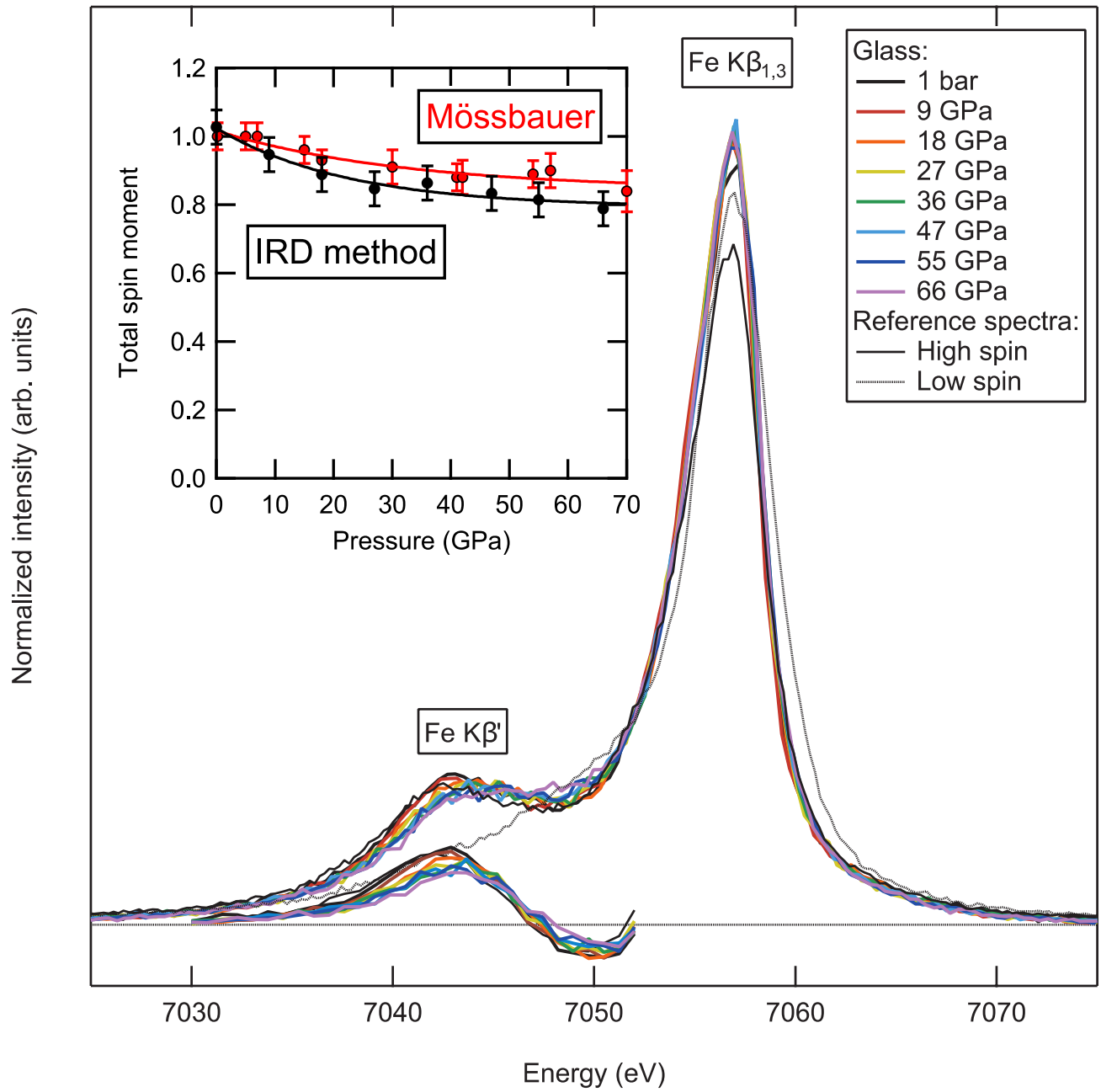
660   **Figure 1**

661
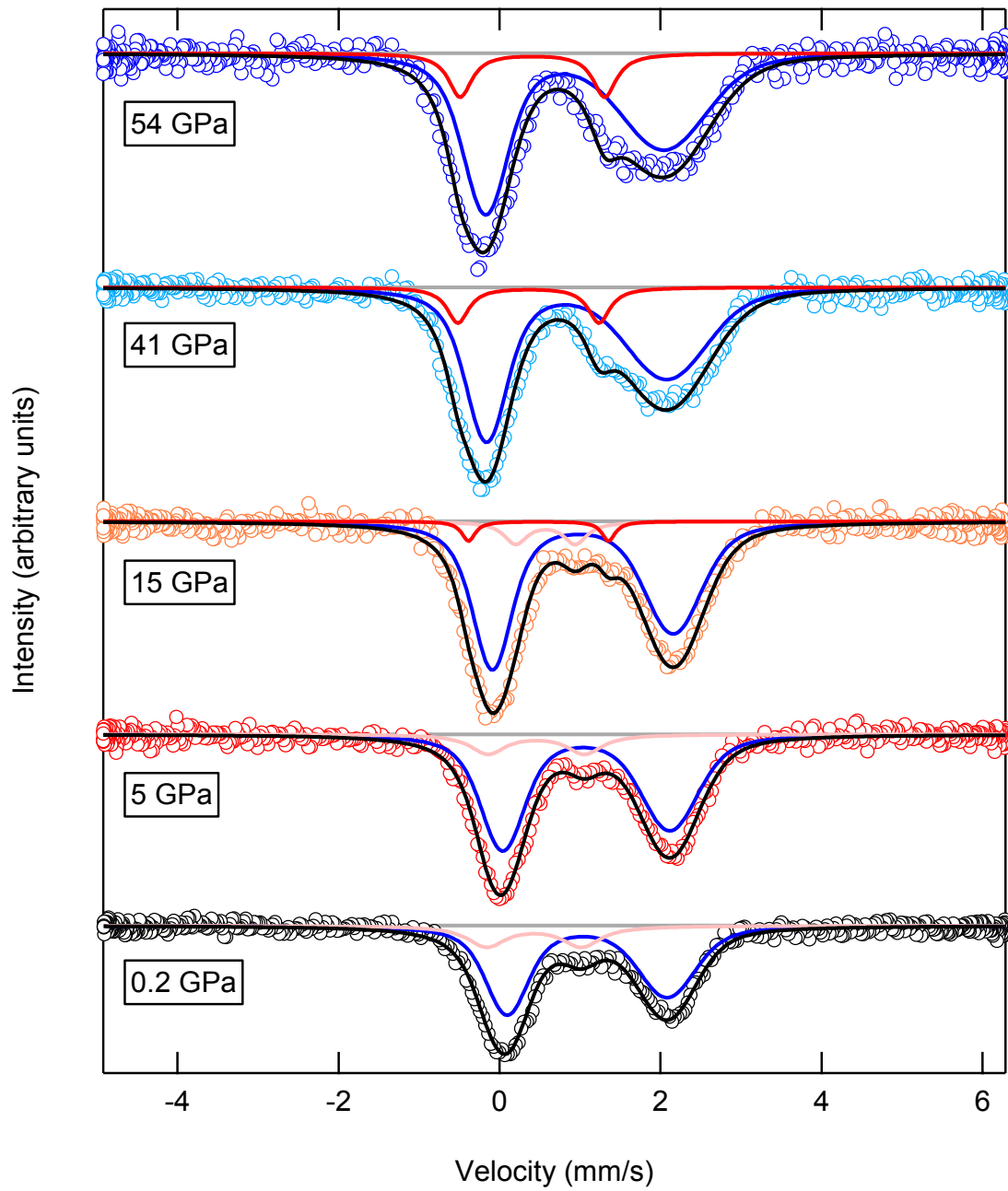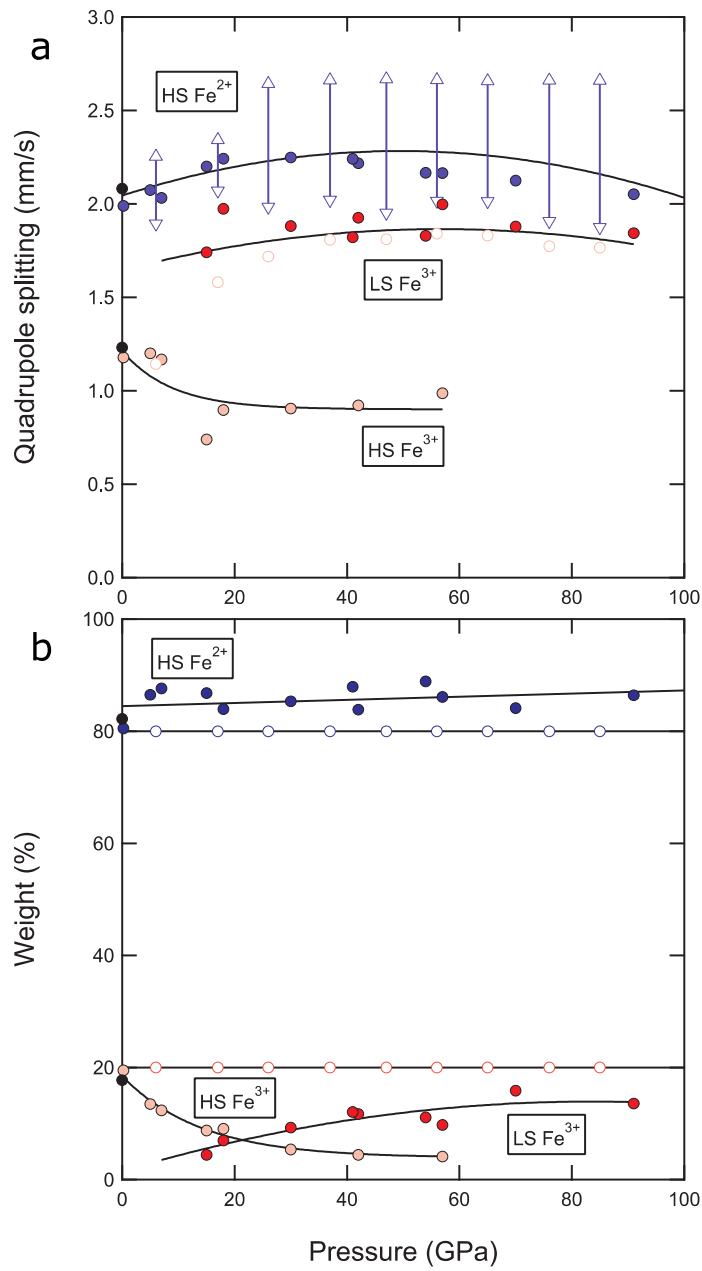
662 **Figure 2**

663

31

664
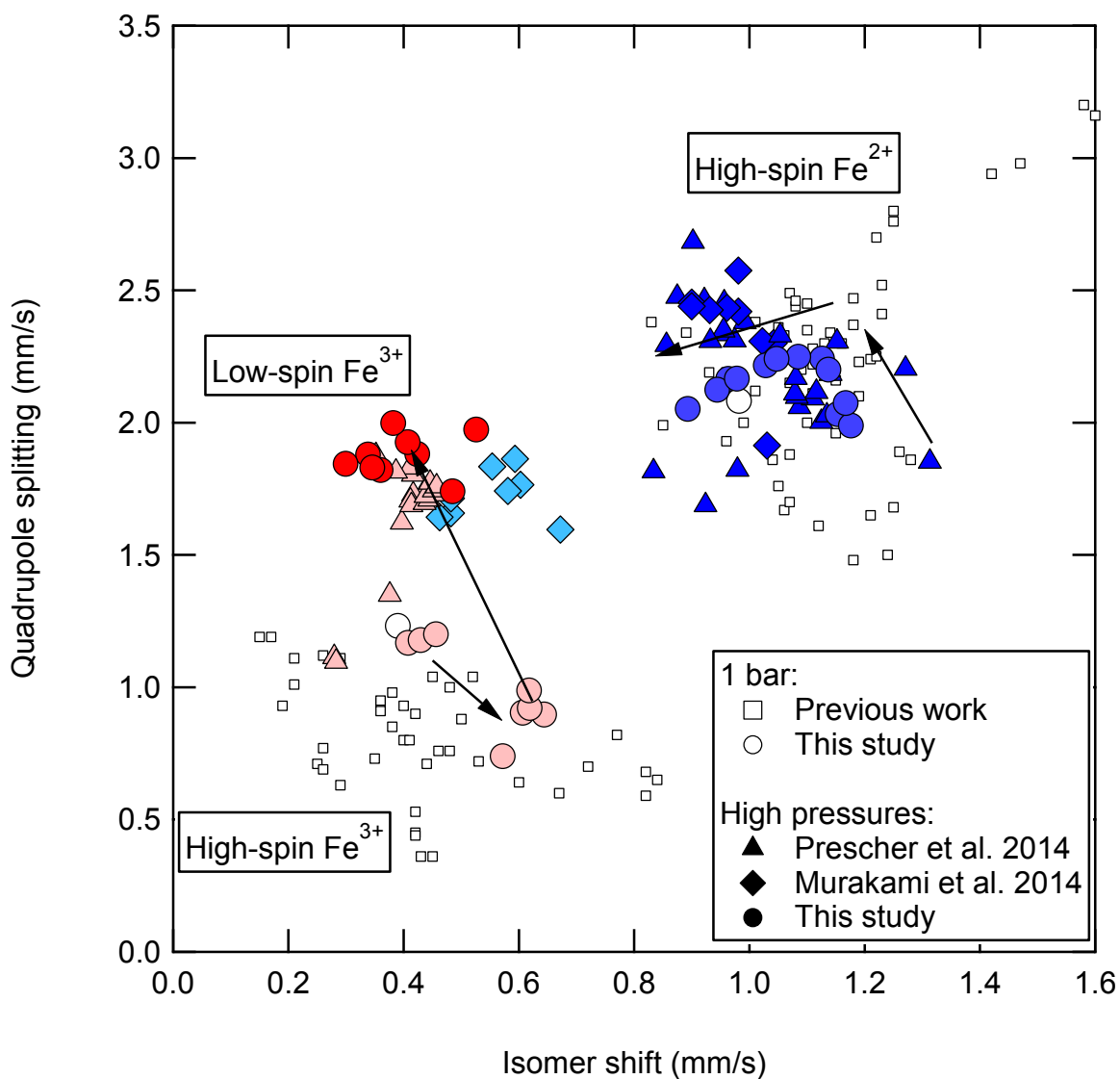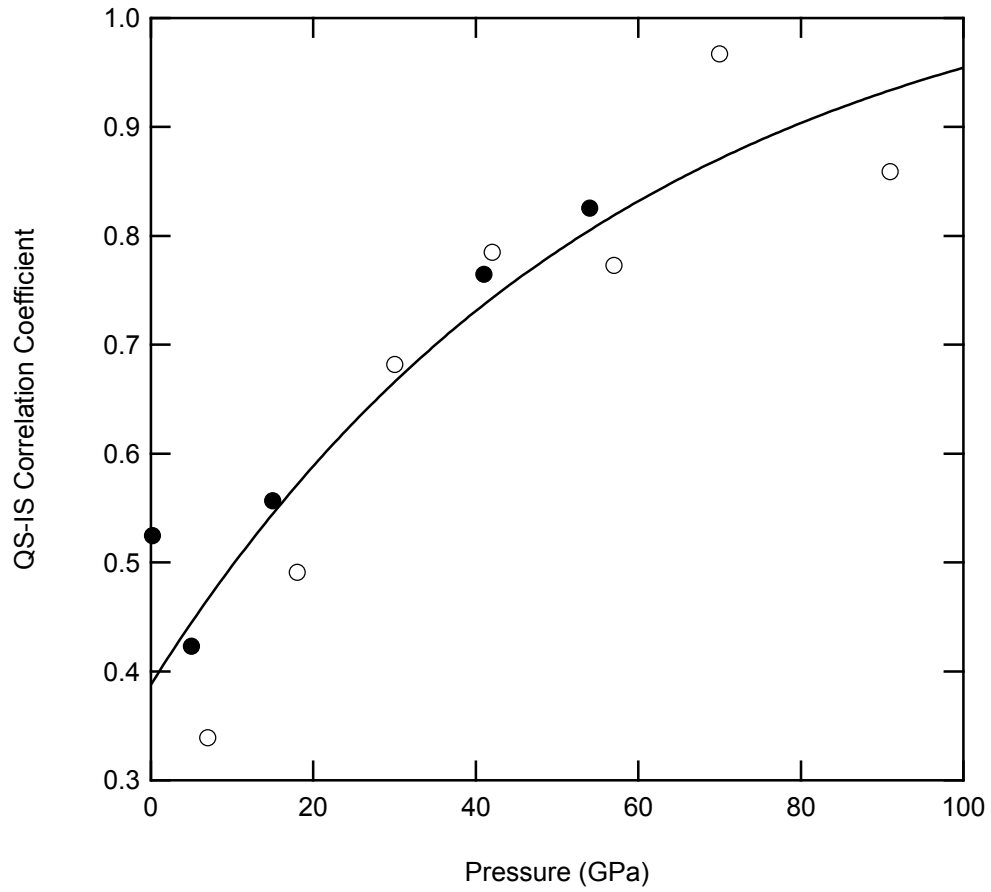
665   **Figure 3**

666

667　**Figure 4**

668

669   **Figure 5**

34

670

671   **Figure 6**

672

673   **Figure 7**

36